14th International Symposium on Turbulence and Shear Flow Phenomena (TSFP14)
Heidelberg, Germany, July 28–31, 2026

HEAT TRANSFER EFFICIENCY IN TURBULENT JET IMPINGEMENT

F. Secchi
Institute of Fluid Mechanics
Karlsruhe Institute of Technology
Karlsruhe, Germany
francesco.secchi@kit.edu

D. Gatti
Institute of Fluid Mechanics
Karlsruhe Institute of Technology
Karlsruhe, Germany
davide.gatti@kit.edu

B. Frohnapfel
Institute of Fluid Mechanics
Karlsruhe Institute of Technology
Karlsruhe, Germany
bettina.frohnapfel@kit.edu

ABSTRACT

The energetic efficiency of heat transfer in a confined turbulent impinging jet at $Re = 5300$ is assessed using direct numerical simulation data. By comparing the advection of fluid internal energy to the dissipated mechanical energy in a closed volume, the analysis reveals that the disparity between heat and momentum transfer renders the thermal energy transfer particularly inefficient.

INTRODUCTION

Jet impingement is a commonplace technique used in cooling applications to achieve localized high heat transfer rates in confined environments. A classical example in this respect is the cooling system inside the blades of gas turbines.

It is well-established in the literature that momentum and heat transfer along the impingement plate show patently dissimilar behaviours. In fact, impinging jets are a classical example in which the Reynolds analogy between heat and momentum transfer breaks (Woodworth *et al.*, 2023).

This is especially true in the stagnation region of the flow, where the incoming free jet gets deflected to develop along the impingement plate. Near the stagnation point, the main cause for momentum deflection comes from the action of an adverse pressure gradient, whereas the wall momentum flux, *i.e.* the wall shear stress, becomes negligibly small over the same region. An analogous mechanism does not exist for the transfer of heat which, in contrast to the momentum wall flux, reaches its maximum in the stagnation region of the flow.

This scenario is well-documented by the numerical study of Wilke & Sesterhenn (2017) and the experimental investigation of Woodworth *et al.* (2023). The fact that the heat transfer greatly exceeds the wall shear stress has given impinging jets the connotation of flows that *favourably* break the Reynolds analogy. However, unlike the case of canonical channel flows (Dipprey & Sabersky, 1963), the degree of similarity between momentum and heat transfer in impinging jets does not provide information about the efficiency of the energy transfer. Indeed, while the integral of the wall heat flux over the impingement plate results in the net thermal power exchanged between the plate and the fluid, a similar connection between the momentum wall flux and the mechanical power required to drive the flow through the system is not as trivial.

Based on this observation, the present study aims at showing an alternative means for assessing the similarity between momentum and heat transfer in flow impingement which carries information about the efficiency of the thermal energy transfer. In particular, we base our analysis on the energy-based approach presented by Secchi *et al.* (2025*b*) to assess momentum and passive-scalar transfer in channel flow, where the mechanical energy budget is compared against the balance equation for $\Gamma = \vartheta^2/2$, where ϑ denotes the non-dimensional scalar temperature field. In this work, we extend this approach to impinging jet flows by using direct numerical simulation (DNS) data of a turbulent impinging jet hitting a smooth target plate.

Methodology

A turbulent jet issues from a fully-developed pipe flow and impinges perpendicularly on a flat plate located at a distance $H = 2D$ from the nozzle exit. The Reynolds number, defined using the nozzle diameter D and the bulk mean velocity U_b, is $Re = 5300$. The Prandtl number of the fluid is fixed at $Pr = 1$. The solenoidal velocity and temperature fields are governed by the incompressible Navier–Stokes equations, supplemented by a convection–diffusion equation for temperature, which is modelled as a passive scalar. At the inlet of the computational domain, fully-developed turbulent inflow conditions are imposed by means of a precursor pipe-flow simulation. No-slip velocity conditions are enforced on both the impingement and confinement plates, while the energy-stable open boundary condition of Dong (2015) is applied on the lateral boundaries for the velocity field. On these open boundaries, the temperature field satisfies the standard zero conductive heat flux condition. The impingement plate is maintained at a constant uniform temperature T_w, whereas the confinement plate is assumed to be in thermal equilibrium with the jet inflow at temperature $T_j < T_w$. Consistently with the boundary conditions enforced on the temperature field, a non-dimensional scalar field is defined as $\theta = (T - T_j)/(T_w - T_j) = (T - T_j)/\Delta T$, where T indicates the fluid temperature, and

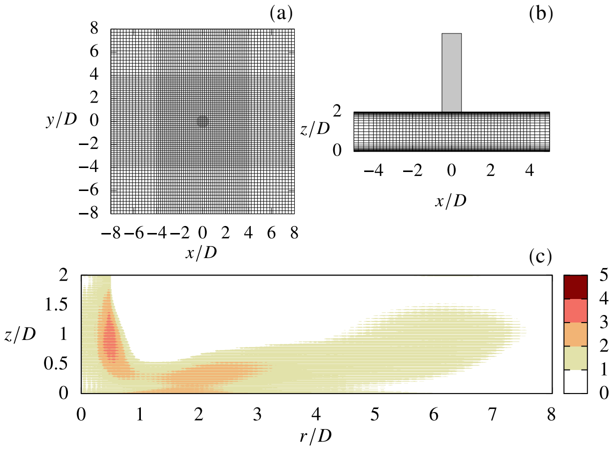

Figure 1. Computational mesh of elements: (a) top view; (b) frontal view, inset for $x \in [-5D, 5D]$. (c) Local grid size to Kolmogorov length scale ratio. Figure adapted from Secchi *et al.* (2025*a*).

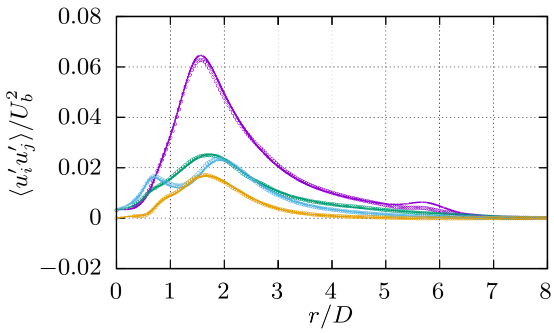

Figure 2. Reynolds stresses radial distributions sampled at $z = 0.1D$. ———, $\langle u_r' u_r' \rangle / U_b^2$; ———, $\langle u_\phi' u_\phi' \rangle / U_b^2$; ———, $\langle u_z' u_z' \rangle / U_b^2$; ———, $\langle u_r' u_z' \rangle / U_b^2$. Solid lines correspond to the computational domain with $L_x = L_y = 16D$; symbols correspond to $L_x = L_y = 20D$. Figure adapted from Secchi *et al.* (2025*a*)

$\Delta T = T_w - T_j$.

The governing equations are integrated numerically using the spectral element method-based solver `Nek5000` (Fisher *et al.*, 2019). The computational mesh of spectral elements is reported in figure 1(a, b). On each element the solution is approximated using Lagrange polynomials of degree $N = 7$ on Gauss-Legendre-Lobatto quadrature nodes. The total number of degrees of freedom is $DOF = 598 \times 10^6$. The grid resolution is compared to the local Kolmogorov length scale in figure 1c.

Time integration is carried out using a semi-implicit approach that combines third-order backward differentiation with extrapolation. The non-linear convective terms in the momentum equations are treated explicitly through third-order extrapolation, whereas the viscous terms are handled implicitly using a third-order backward differentiation scheme. An operator-splitting method is used to separate the pressure and velocity computations. As a result, each time step requires solving a pressure Poisson equation together with a Helmholtz problem for each velocity component. After updating the velocity field, an additional Helmholtz problem is solved for each passive scalar. Once the flow has reached a statistically steady state, time-averaged statistics are collected over an interval of approximately $T_{avg} \approx 500, D/U_b$.

The use of an artificial open boundary prompts the question of whether the computational domain size affects the resulting flow statistics. To assess this, an additional simulation with comparable resolution was conducted in an enlarged domain with dimensions $L_x = 20D$ and $L_y = 20D$. Although this case was integrated over a shorter time interval to limit computational cost, the statistical quantities obtained show close agreement with those from the smaller domain. This indicates that the results are insensitive to the position of the artificial open boundary. As an example, Fig. 2 presents the radial profiles of the Reynolds stresses evaluated at a wall-normal location of $z = 0.1D$, where the prime notation denotes fluctuations relative to the combined time and azimuthal mean.

Temporal and spatial averaging in the azimuthal direction, ϕ, is denoted with angular brackets, $\langle \cdot \rangle$, throughout the text. A prime superscript is used to indicate fluctuations with respect to the time- and spatial-mean value. The combined time- and azimuthally-averaged flow field is represented as a two-dimensional distribution in terms of the radial distance from the jet axis r and the wall-normal coordinate z.

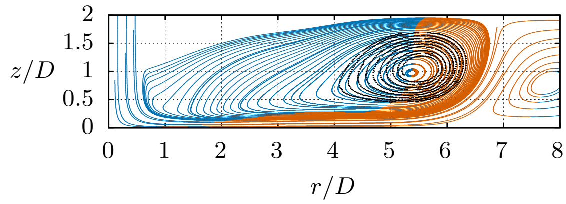

Figure 3. Selected streamlines of the mean flow field. Streamlines are colour-coded to evidence areas of positive (orange) and negative (blue) wall-normal velocity, $\langle u_z \rangle / U_b$. Black dots correspond to data from Chen *et al.* (2024). Figure adapted from Secchi *et al.* (2025*a*).

RESULTS

A large-scale recirculating structure characterizes the mean flow field, as it is shown in figure 3 through selected streamlines. In the figure, the streamlines are colour-coded according to the sign of the local wall-normal velocity, $\langle u_z \rangle$. In the stagnation region, *i.e.* for small radial distances, the near-wall region is characterized by fluid moving towards the wall; further downstream, as the flow develops along the impingement plate, positive mean wall-normal velocity characterizes the near wall region as a consequence of the thickening of the boundary layer. At large radial distances, for $r \gtrsim 5D$, the flow lifts up from the wall and recirculates back in the large-scale cell. This mechanism continually brings warm fluid in the bulk of the flow and, due to the recirculation, mixes it with the fresh cold fluid incoming from the free jet.

A similar scenario has been observed also in the literature. Along with the present DNS data, figure 3 shows streamlines from Chen *et al.* (2024), who conducted PIV measurements of a non-confined impinging jet at a similar Reynolds number. The agreement between the centres location of the large-scale recirculating cells is qualitatively good between the present DNS and the PIV measurements.

Because $\langle u_r \rangle$ and $\langle \theta \rangle$ have different boundary values at the impingement and confinement plates, their mean distributions exhibit pronounced differences throughout the domain.

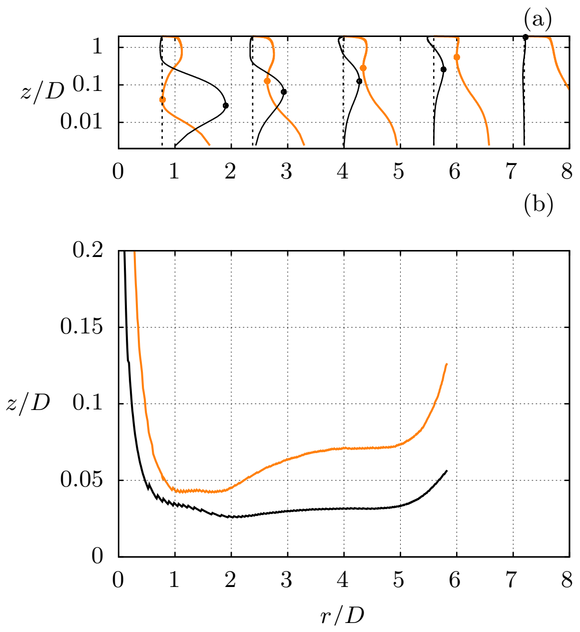

Figure 4. (a) Mean radial velocity and temperature profiles at different radial locations. ———, $\langle u_r \rangle / U_b$; ———, $\langle \theta \rangle$; symbols indicate the maxima and minima of, respectively, the mean radial velocity and temperature profiles. Vertical black dashed lines indicate the radial location at which the profiles are sampled. (b) Boundary layer thicknesses. ———, z_m/D; ———, $z_{\theta m}/D$. Figure adapted from Secchi *et al.* (2025*a*).

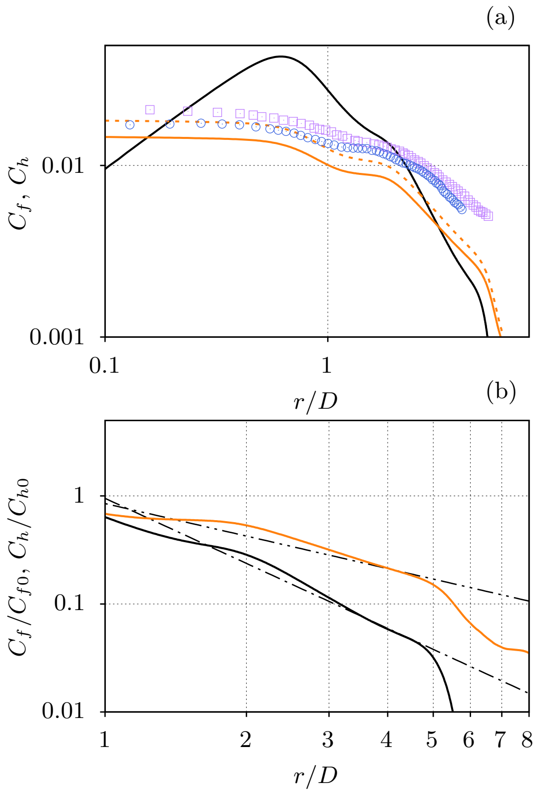

Figure 5. Mean friction coefficient and Stanton number distributions. (a) ———, C_f; ———, C_h with $Pr = 1$; - - - - -, C_h with $Pr = 0.7$; ⊙, Lee & Lee (2000); ⊡, Katti *et al.* (2011). (b) ———, C_f/C_{f0}; ———, C_h/C_{h0}; dash-dot line, $\sim (r/D)^{-2}$; dash-dot-dot line, $\sim (r/D)^{-1}$. Figure adapted from Secchi *et al.* (2025*a*).

Within the wall jet developing along the lower plate, the incoming high-momentum, low-temperature fluid from the jet core leads to temperature minima occurring in the same region where the radial velocity reaches its maximum. In contrast, in the upper region, the recirculating motion transports warmer fluid along the confinement plate.

As shown in Fig. 4a, in the wall jet the location of the maximum mean radial velocity, u_m, and that of the minimum mean scalar, θ_m, are separated in the wall-normal direction, occurring at z_m and $z_{\theta m}$, respectively. Notably, the offset $z_{\theta m} - z_m > 0$ increases with radial distance from the jet axis. This behaviour, which is further depicted in figure 4b, contrasts with the expectation for a unit Prandtl number, where the velocity and thermal boundary layer thicknesses would typically be of similar magnitude.

The wall heat transfer along the impingement plate is reported in figure 5a through the Stanton number distribution, $C_h = q_w/(\rho c_p \Delta T U_b)$, where c_p indicates the fluid heat capacity at constant pressure, and q_w denotes the mean wall-heat flux as a function of the radial coordinate. Two Stanton number distributions are reported for two different Prandtl numbers: namely $Pr = 1$, and $Pr = 0.7$. The latter one serves as support to the validation of the present numerical framework through the comparison with available experimental data, which use air as working fluid. In fact figure 5a also reports experimental data from Lee & Lee (2000) and Katti *et al.* (2011). A good agreement is found between the present C_h distribution for $Pr = 0.7$ and the literature data. The observed differences, which occur predominantly at large radial distances from the jet axis, can be ascribed to slightly different inflow conditions (*e.g.* fully developed turbulent jet and Reynolds number), different temperature boundary conditions at the impingement plate, and the presence of a confinement plate in the DNS data (not present in both experiments). The latter prevents the entrainment of cold fluid from the outside environment, thus producing an overall warmer environment and determining a lower heat transfer at the impingement plate.

Figure 5a also reports the distribution of the friction coefficient along the impingement plate, $C_f = 2\tau_w/(\rho U_b^2)$, where τ_w indicates the mean wall-shear stress as a function of the radial coordinate. In the stagnation region, the wall heat flux attains its maximum value, while the skin-friction coefficient tends to zero as the radial distance decreases. Here, the mean momentum and thermal fields exhibit markedly different behaviour. The flow deflection, which redistributes wall-normal momentum into the radial direction, is driven by the pressure field and therefore has no direct influence on the temperature field.

As the fluid accelerates radially, the skin-friction coefficient increases rapidly with r, reaching a peak at approximately $r \approx D/2$, and subsequently decreases as the flow spreads and decelerates. Flow separation occurs around $r \approx 5.8D$, beyond which the skin-friction coefficient becomes negative. In contrast, the Stanton number decreases monotonically from the stagnation point, except in the range $r \approx 1.5D$–$2D$, where a local increase is observed. A similar trend is also visible in C_f over this interval. Previous studies (e.g., Dairay *et al.*, 2015) attribute this feature to a secondary enhancement of heat transfer caused by the unsteady interaction of coherent vortical structures with the wall. Under the present conditions, however, this secondary peak remains weakly developed. Further downstream, the profiles of C_f and C_h become more alike, although for $r \gtrsim 3D$ the magnitude of C_h exceeds that of C_f. Near and beyond the separation point, the two quantities again diverge significantly.

Normalizing C_f and C_h by their respective maxima along the impingement plate, C_{f0} and C_{h0}, highlights differences in the evolution of wall shear and heat transfer along the plate. As shown in figure 5b, in the wall-jet region ($2D \lesssim r \lesssim 5D$), both C_f and C_h follow an approximate power-law decay, consistent with the experimental findings of Woodworth *et al.* (2023). Despite their comparable magnitudes, their radial decay rates differ significantly. As discussed by Secchi *et al.* (2025*a*) and Secchi (2025), this difference can be readily explained based on the order of magnitude analysis of the radial momentum equation and of the passive-scalar transport-diffusion equation. Namely, assuming $u_m \sim const/r$ (due to mass conservation) and $\theta_m \sim const.$, and applying these ansatz to the momentum and scalar governing equations, results in $C_f \sim r^{-2}$ and $C_h \sim r^{-1}$. As seen in figure 5b, these estimates are approximately well captured by the present data over the range $3D \lesssim r \lesssim 5D$.

Although the spatial distribution of the mean heat transfer coefficient directly quantifies the thermal power exchanged at the impingement surface, the mean skin-friction coefficient does not provide an equally direct measure of the mechanical power required to sustain the flow. To address this point, we examine the transport equation for the total mechanical energy, defined as $\mathscr{B} = \mathbf{u}\cdot\mathbf{u}/2 + p/\rho$. This relation is obtained by taking the inner product of the momentum equation with the velocity vector and applying standard vector identities.

Upon performing time and spatial averaging, the resulting mean balance equation can be written as (Secchi *et al.*, 2025*b*):

$$\nabla\cdot\langle\mathbf{u}\mathscr{B}\rangle = \nu\nabla^2\langle\mathscr{B}\rangle - \nu\langle\boldsymbol{\omega}\cdot\boldsymbol{\omega}\rangle, \tag{1}$$

where $\boldsymbol{\omega}$ denotes the vorticity vector, ν is the kinematic viscosity of the fluid, and $\nu\langle\boldsymbol{\omega}\cdot\boldsymbol{\omega}\rangle$ corresponds to the mean rate of mechanical energy dissipation.

The integration of (1) over the flow domain allows to relate the mechanical energy consumption to the power input to the system. For a cylindrical control volume, $\mathscr{V}$, of radius r, whose bottom and top surfaces correspond, respectively, to the impingement and top plates of the flow domain, and whose axis of symmetry coincides with the jet axis, the net mechanical energy balance reads: $\Pi_{out} - \Pi_{in} = -\mathscr{E}$, where $\Pi_{out} = \int_0^H 2\pi r\langle\mathscr{B}u_r\rangle\Big|_{\xi=r,z}\mathrm{d}z$ is the mechanical energy convected through the lateral surface of the control volume, $\Pi_{in} = -\int_0^{D/2} 2\pi\xi\langle u_z\mathscr{B}\rangle\Big|_{\xi,z=H}\mathrm{d}\xi$ is the power input across the jet nozzle, and the mean bulk dissipation of mechanical energy is $\int_0^H\int_0^r 2\pi\xi\,\nu\langle\boldsymbol{\omega}\cdot\boldsymbol{\omega}\rangle\,\mathrm{d}\xi\mathrm{d}z$.

Figure 6 reports the integral budget terms of equation (1) computed for control volumes $\mathscr{V}$ of increasing radial size, starting from a minimum radius of $r = D/2$. The power supplied to the system, Π_{in}, is set by the prescribed inflow conditions at the nozzle exit. As the radial distance increases, this input power is progressively dissipated within the flow, contributing to the cumulative energy loss $\mathscr{E}$ and thereby reducing the remaining mechanical power, Π_{out}, available to sustain the downstream motion.

In the range $3D \lesssim r \lesssim 5D$, Π_{out} follows a clear power-law decay, $\Pi_{out} \sim r^{-2}$. This trend can be interpreted by noting that

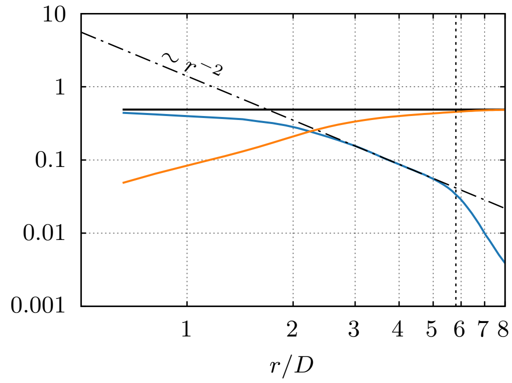

Figure 6. Mechanical energy integral budgets. $\Pi_{in}/(U_b^3D^2)$; $\Pi_{out}/(U_b^3D^2)$; $\mathscr{E}/(U_b^3D^2)$. A vertical black-dashed line indicates the radial location of flow separation on the impingement plate. Figure adapted from Secchi *et al.* (2025*a*).

the mean convective transport of mechanical energy, $\langle\mathscr{B}u_r\rangle$, is expected to scale as $u_m^3 \sim r^{-3}$, consistent with the argument that, due to mass conservation, the mean radial velocity is expected to decay as $\sim const./r$.

Beyond the separation point (which is marked with a vertical dashed line in figure 6), for $r \gtrsim 5.8D$, the decay becomes significantly steeper, with Π_{out} approaching zero approximately as $\Pi_{out} \sim r^{-7}$.

The heat transfer efficiency, η, is then obtained by comparing the net heat conduction across the control volume boundary, $\partial\mathscr{V}$, and the consumed mechanical energy, $\mathscr{E}$; namely, assuming a negligible molecular heat flux across the lateral surface of the control volume, the heat transfer efficiency can be written as $\eta = (\Pi_\theta - \Pi_{\theta T})/\mathscr{E}$, where $\Pi_\theta = -c_p\Delta T\int_0^r 2\pi\xi\,\alpha\langle\theta\rangle_{,z}\Big|_{\xi,z=0}\mathrm{d}\xi$ and $\Pi_{\theta T} = -c_p\Delta T\int_0^r 2\pi\xi\,\alpha\langle\theta\rangle_{,z}\Big|_{\xi,z=H}\mathrm{d}\xi$ are, respectively, the net heat exchanged across the bottom and top faces of the control volume.

The radial variation of η is shown in figure 7a. At small radial distances, the heat flux through the confinement plate is negligible compared with that at the impingement surface. Under these conditions, the heat transfer efficiency can be approximated as $\eta \approx \Pi_\theta/\mathscr{E}$. From the figure, it can be seen that this approximation is appropriate for $r \lesssim 4D$. At larger radii, however, the heat fluxes at the two plates become comparable, and the approximation departs significantly from the reference expression.

Although the approximation $\eta \approx \Pi_\theta/\mathscr{E}$ remains useful at small r, it should be noted that Π_θ includes a contribution, $\Pi_{\theta B}$, associated with the imposed temperature difference between the impingement and confinement plates. This component would exist even in the absence of fluid motion, in which case the mechanical energy input vanishes and η becomes undefined. To address this, $\Pi_{\theta B}$ can be subtracted from Π_θ in the approximate expression for η. As shown in figure 7a, this correction has only a minor effect for the present configuration across all radial positions.

Overall, the radial distribution of η indicates that the thermal efficiency remains well below unity for all considered control volumes $\mathscr{V}$. This suggests that jet impingement is not an energetically efficient mechanism for heat removal, although high heat transfer rates occur in the stagnation region

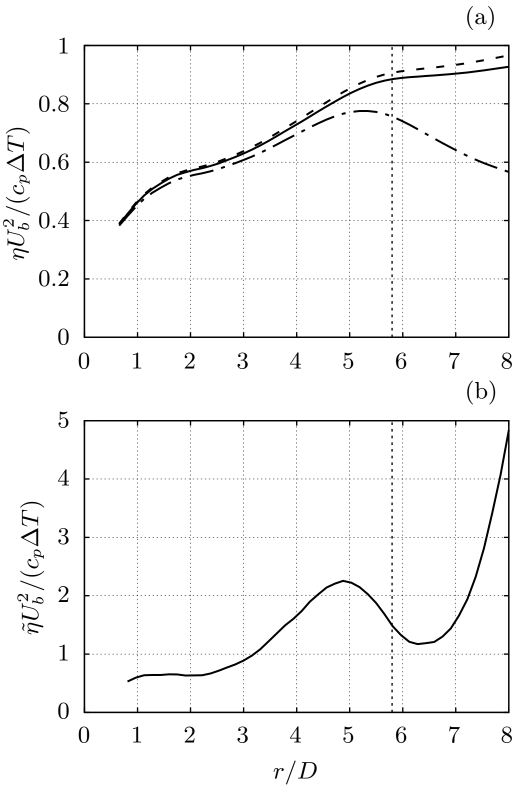

Figure 7. (a) Dash-dot line, thermal transfer efficiency $\eta U_b^2/(c_p \Delta T)$; dashed-line, $U_b^2 \Pi_\theta/(c_p \Delta T \mathscr{E})$; solid line, $U_b^2(\Pi_\theta - \Pi_{\theta B})/(c_p \Delta T \mathscr{E})$. (b) Local thermal transfer efficiency, $\tilde{\eta} U_b^2/(c_p \Delta T)$. In both panels, a vertical black dashed line indicates the radial location of flow separation on the impingement plate. Figure adapted from Secchi *et al.* (2025*a*).

for a vanishingly small wall shear stress (Bunker, 2013; Rouhi *et al.*, 2022). Indeed, as discussed in reference to figure 5, for $r \lesssim D/2$ the wall heat flux significantly exceeds the wall momentum flux. However, these elevated heat transfer rates are achieved at the expense of high mechanical energy input, leading to low efficiency values, with $\eta U_b^2/(c_p \Delta T) < 0.6$ for $r \lesssim 2.5D$.

To obtain spatially localized information from the integral balances, the analysis can be applied to control volumes defined as hollow cylindrical shells, coaxial with the jet axis and bounded by the impingement and confinement plates. The volume of such a shell is defined as $[\mathscr{V}] = \mathscr{V}(r + \Delta r/2) - \mathscr{V}(r - \Delta r/2)$, where $[\cdot]$ denotes the difference between quantities evaluated over adjacent cylindrical volumes, and Δr is an arbitrary radial increment. With this definition, the balance equation for$\langle \mathscr{B} \rangle$ over $[\mathscr{V}]$ reduces to $[\Pi_{out}] = -[\mathscr{E}]$.

A localized measure of the energetic efficiency of heat transfer enhancement within $[\mathscr{V}]$ is given by $\tilde{\eta} = c_p \Delta T \left[\Pi_\theta - \Pi_{\theta_B}\right] / [\mathscr{E}]$, as shown in figure 7b. For $r \lesssim 3D$, the flow-induced heat transfer enhancement is energetically inefficient, as the mechanical energy dissipated within $[\mathscr{V}]$ significantly exceeds the additional thermal power transferred at the wall. At larger radii, $\tilde{\eta}$ exceeds unity and reaches a local maximum of approximately 2.3 at $r \approx 5D$. This indicates that, in the wall-jet region ($r \gtrsim 3D$), relatively low mechanical dissipation is associated with a comparatively strong enhancement of wall heat transfer.

Beyond this peak, as the flow approaches separation, $\tilde{\eta}$ decreases, reaching a minimum value of about 1.3 downstream of the separation point. Further downstream ($r \gtrsim 6.5D$), the available mechanical energy becomes very small, while a noticeable heat transfer enhancement persists, leading to a sharp increase in $\tilde{\eta}$.

A comparison of figures 3 and 7b suggests a link between near-wall mean flow and the local heat transfer efficiency, $\tilde{\eta}$. Regions where the near-wall flow is directed toward the wall, *i.e.* where $\langle u_z \rangle < 0$, are associated with low values of $\tilde{\eta}$. In these regions, strong wall-normal transport enhances heat transfer but also increases the mechanical energy dissipation. Conversely, for $r \gtrsim 2D$, where the near-wall flow is directed away from the wall ($\langle u_z \rangle > 0$) due to boundary layer growth, the local efficiency increases. In this case, reduced heat transfer rates are accompanied by lower mechanical energy dissipation.

CONCLUSIONS

This study examines heat transfer in a turbulent jet impinging perpendicularly onto a smooth plate maintained at a uniform temperature different from that of the jet. The flow is treated as incompressible, and temperature is modelled as a passive scalar, neglecting buoyancy effects. A unit Prandtl number is considered to enable direct comparison between heat and momentum transport.

Direct numerical simulation is employed to fully resolve the turbulent flow at a Reynolds number $Re = 5300$, based on the jet bulk velocity U_b and nozzle diameter D. The inflow is obtained from a precursor simulation of fully developed pipe flow at $Re_\tau = 180$. The jet impinges on a plate located at $H = 2D$, while a second, isothermal confinement plate at nozzle height encloses the domain.

The mean flow features a large recirculating cell extending several diameters radially, with its centre around $r \approx 5.4D$, sustained by momentum transport from the wall jet. Along the impingement surface, the velocity and thermal boundary layers exhibit distinct behaviour, with the thermal layer becoming significantly thicker downstream.

The radial distributions of the skin-friction coefficient, C_f, and of the Stanton number, C_h, differ markedly. For $r \gtrsim 3D$, both follow power-law trends, with $C_f \sim r^{-2}$ and $C_h \sim r^{-1}$, indicating a faster decay of momentum transfer compared to heat transfer.

An integral energy analysis is conducted by applying the time- and azimuthally averaged transport equation for total mechanical energy—defined as the sum of kinetic energy and pressure work—over cylindrical control volumes $\mathscr{V}$, coaxial with the jet and of radius r. This balance shows that the net mechanical energy expenditure within $\mathscr{V}$ is entirely accounted for by viscous dissipation, $\mathscr{E}$, obtained as the volume integral of the mean dissipation field $\nu \langle \boldsymbol{\omega} \cdot \boldsymbol{\omega} \rangle$.

By evaluating this balance for control volumes of increasing size, the thermal efficiency is quantified as the ratio between the flow-induced heat transfer at the impingement surface and the mechanical power required to sustain the flow. The results indicate that, for any radial size of the control volumes considered, the dissipated mechanical energy exceeds the corresponding thermal power transfer. This demonstrates that the additional heat removal enabled by the impinging jet is consistently outweighed by the energetic cost of maintaining the flow.

ACKNOWLEDGMENTS

This work was supported by the German Research Foundation (DFG) under the Collaborative Research Centre TRR150 (project number 237267381). The simulations were performed on the HPE Apollo (Hawk) supercomputer at the High Performance Computing Center Stuttgart (HLRS) under the grant number 44198.

REFERENCES

Bunker, R. S. 2013 Gas Turbine Cooling: Moving From Macro to Micro Cooling. *Turbo Expo: Power for Land, Sea, and Air*, vol. Volume 3C: Heat Transfer, p. V03CT14A002.

Chen, M., Yang, L., Huang, H., Zhou, X., Zhang, W. & Wang, D. 2024 Flow characteristics in a semi-confined circular-pipe impinging jet. *Phys. Fluids* **36** (2), 025108.

Dairay, F., Fortuné, V., Lamballais, E. & Brizzi, L. E. 2015 Direct numerical simulation of a turbulent jet impinging on a heated wall. *J. Fluid Mech.* **764**, 362–394.

Dipprey, D. F. & Sabersky, R. H. 1963 Heat and momentum transfer in smooth and rough tubes at various prandtl numbers. *Int. J. Heat Mass Transfer* **6** (5), 329–353.

Dong, S. 2015 A convective-like energy-stable open boundary condition for simulations of incompressible flows. *J. Comp. Phys.* **302**, 300–328.

Fisher, P. F., Lottes, J. W. & Kerkemeier, S. G. 2019 NEK5000 Version 19.0 Argonne National Laboratory, Illinois.

Katti, V. V., Yasaswy, S. N. & Prabhu, S. V. 2011 Local heat transfer distribution between smooth flat surface and impinging air jet from a circular nozzle at low Reynolds numbers. *Heat Mass Transf.* **47** (3), 237–244.

Lee, J. & Lee, S. J. 2000 The effect of nozzle configuration on stagnation region heat transfer enhancement of axisymmetric jet impingement. *Int. J. Heat and Mass Transf.* **43** (18), 3497–3509.

Rouhi, A., Endrikat, S., Modesti, D., Sandberg, R. D., Oda, T., Tanimoto, K., Hutchins, N. & Chung, D. 2022 Riblet-generated flow mechanisms that lead to local breaking of reynolds analogy. *J. Fluid Mech.* **951**, A45.

Secchi, F. 2025 Passive-scalar transfer in complex turbulent flows. PhD thesis, Karlsruher Institut für Technologie (KIT).

Secchi, F., Gatti, D., & Frohnapfel, B. 2025*a* Energetics of a turbulent impinging jet with passive scalar transport. *J. Fluid Mech. (Under review)* .

Secchi, F., Gatti, D., Piomelli, U. & Frohnapfel, B. 2025*b* A framework for assessing the reynolds analogy in turbulent forced convection over rough walls. *J. Fluid Mech.* **1006**, R3.

Wilke, R. & Sesterhenn, J. 2017 Statistics of fully turbulent impinging jets. *J. of Fluid Mech.* **825**, 795–824.

Woodworth, A. D., Salazar, D. M. & Liu, T. 2023 Heat transfer and skin friction: Beyond the Reynolds analogy. *Int. J. Heat Mass Transfer* **206**, 123960.